Biophysical Journal
Article

Biophysical Society

One-Way Allosteric Communication between the Two Disulfide Bonds in Tissue Factor

Beifei Zhou,[1,2] Philip J. Hogg,[3] and Frauke Gräter[2,4,*]
[1]CAS-MPG Partner Institute and Key Laboratory for Computational Biology (PICB), Shanghai, China; [2]Heidelberg Institute for Theoretical Studies, Heidelberg, Germany; [3]The Centenary Institute and National Health and Medical Research Council Clinical Trials Centre, University of Sydney, Sydney, Australia; and [4]University of Heidelberg, Interdisciplinary Center for Scientific Computing, Heidelberg, Germany

ABSTRACT Tissue factor (TF) is a transmembrane glycoprotein that plays distinct roles in the initiation of extrinsic coagulation cascade and thrombosis. TF contains two disulfide bonds, one each in the N-terminal and C-terminal extracellular domains. The C-domain disulfide, Cys186-Cys209, has a −RHStaple configuration in crystal structures, suggesting that this disulfide carries high pre-stress. The redox state of this disulfide has been proposed to regulate TF encryption/decryption. Ablating the N-domain Cys49-Cys57 disulfide bond was found to increase the redox potential of the Cys186-Cys209 bond, implying an allosteric communication between the domains. Using molecular dynamics simulations, we observed that the Cys186-Cys209 disulfide bond retained the −RHStaple configuration, whereas the Cys49-Cys57 disulfide bond fluctuated widely. The Cys186-Cys209 bond featured the typical −RHStaple disulfide properties, such as a longer S-S bond length, larger C-S-S angles, and higher bonded prestress, in comparison to the Cys49-Cys57 bond. Force distribution analysis was used to sense the subtle structural changes upon ablating the disulfide bonds, and allowed us to identify a one-way allosteric communication mechanism from the N-terminal to the C-terminal domain. We propose a force propagation pathway using a shortest-pathway algorithm, which we suggest is a useful method for searching allosteric signal transduction pathways in proteins. As a possible explanation for the pathway being one-way, we identified a pronounced lower degree of conformational fluctuation, or effectively higher stiffness, in the N-terminal domain. Thus, the changes of the rigid domain (N-terminal domain) can induce mechanical force propagation to the soft domain (C-terminal domain), but not vice versa.

INTRODUCTION

Tissue factor (TF) is the plasma membrane cofactor for coagulation factor VIIa. Binding of VIIa to TF leads to activation of factor X by discrete proteolysis to initiate blood coagulation, which stabilizes the developing thrombus. TF is present on circulating monocytes and neutrophils in a mostly non-coagulant or cryptic form bound non-productively to VIIa, and acute events lead to local decryption of TF and productive binding of VIIa (1). The mechanism of decryption of TF remains controversial, but it appears to involve both exposure of phosphatidylserine on the cell surface and formation of a disulfide bond between unpaired Cys186 and Cys209 in TF.

The current evidence implies that cryptic TF is maintained by a neutral phospholipid environment and by factors that keep TF cysteine residues 186 and 209 in the reduced free-thiol form. Both the thioredoxin/thioredoxin reductase/NADPH system (2) and S-glutathionylation (3) or S-nitrosylation (4,5) of the Cys209 thiol have been implicated in maintaining TF in a reduced form. TF is decrypted by activation of a purinergic receptor (P2X7) or complement (C5b-7) on myeloid cells, and protein disulfide isomerase (PDI) has been implicated in both systems (6). PDI can oxidize the Cys186/Cys209 dithiol directly (7), but may also be involved in removing glutathione and/or NO from Cys209 (1).

Full-length TF consists of extracellular (residues 1–219), transmembrane (residues 220–242), and cytoplasmic (residues 243–263) domains (8). The crystal structure of the extracellular region of human TF has been resolved (PDB: 1boy and residues 3–213) (9). There are two disulfide bonds: the N-terminal Cys49-Cys57 and the C-terminal Cys186-Cys209 (10) (Fig. 1 *A*). The Cys186-Cys209 bond has the typical feature of a −RHStaple disulfide bond, linking adjacent antiparallel β-strands (11–15), which suggests that the Cys186-Cys209 bond is an allosteric disulfide bond (16). The classification of disulfide bonds is based on the signs of the five χ_i dihedral angles, and the −RHStaple type of disulfide bonds are defined by the

Submitted September 19, 2016, and accepted for publication December 1, 2016.

*Correspondence: frauke.graeter@h-its.org

Editor: Amedeo Caflisch,

http://dx.doi.org/10.1016/j.bpj.2016.12.003

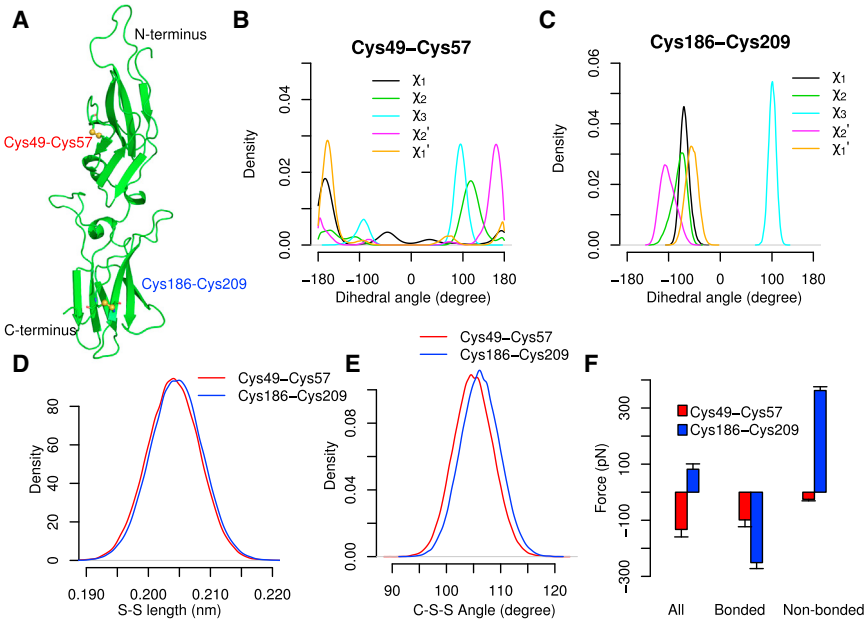

FIGURE 1 Structural and mechanical properties of disulfide bonds in TF. (*A*) Structure of TF, with the N-terminal Cys49-Cys57 and the C-terminal Cys186-Cys209 bonds shown as sticks and the sulfur atoms shown as spheres. (*B* and *C*) Distributions of the five dihedral angles χ_1, χ_2, χ_3, χ_2', and χ_1' of the Cys49-Cys57 and Cys186-Cys209 disulfides, respectively. (*D*) S-S bond lengths in Cys49-Cys57 (*red*) and Cys186-Cys209 (*blue*). (*E*) C-S-S angles in Cys49-Cys57 (*red*) and Cys186-Cys209 (*blue*). (*F*) Prestress of the disulfide bonds between two cysteine residues in TF, for Cys49-Cys57 (*red*) and Cys186-Cys209 (*blue*), showing the force for all interactions (*left*), bonded interactions (*middle*), and nonbonded interactions (*right*). To see this figure in color, go online.

signs −, −, +, −, − (11,16). Prestress represents the internal mechanical balance between tension and compression of the residue-residue interactions in a protein at equilibrium condition, and it can be related to the intrinsic mechanical properties of a protein (17). The particular geometry of the −RHStaple disulfide bond was observed to store high prestress due to stretched bonds and angles around the S-S bond, which is considered to increase reactivity (16).

Liang et al. (18) discovered that ablation of the Cys49-Cys57 disulfide in the N-terminal domain increased the redox potential of the Cys186-Cys209 disulfide by 36 mV, which hints at an allosteric communication between the two disulfide bonds in TF activation. Although the Cys49-Cys57 disulfide is buried and not known to be reduced in vivo, this long-range communication is an intriguing case of protein allostery that merits further examination. Long-range allostery forms the basis of many cases of protein regulation, but the underlying mechanisms often cannot be inferred from static protein structures (19). Molecular dynamics (MD) simulations have become a highly valuable tool for understanding protein allostery (20). In contrast to analysis methods based on changes in protein conformation and dynamics, the MD-based method recently devised by us, termed force distribution analysis (FDA), monitors changes in protein molecular forces to examine allostery (21). FDA profits from the high sensitivity of forces to even minor conformational changes, and has proved valuable to study allosteric pathways in diverse proteins, such as gene expression factors or chaperones (22,23).

To understand the allosteric mechanism connecting the two disulfide bonds in TF, we performed all-atom equilibrium MD simulations and FDA on the fully oxidized form, TF(SS | SS), and on molecules where the N- or C-terminal disulfides were ablated by mutating both Cys residues to Ala, TF(AA | SS) or TF(SS | AA), respectively. We first analyzed the configuration and prestress properties of the two disulfide bonds in the oxidized wild-type TF(SS | SS). We also confirmed dynamically, using MD simulations, that Cys186-Cys209 prefers a −RHStaple disulfide with the signs of the five dihedral angles −, −, +, −, − (Fig. 1 *C*). Using FDA (21,24–26), we show that the Cys186-Cys209 bond is highly stressed as expected (16). Indeed, the mutation of the N-terminal Cys49-Cys57 bond gives rise to a change in inter-residue forces all the way up to the C-terminal Cys186-Cys209 bond. However, the mutation of the C-terminal Cys186-Cys209 bond caused comparably local force changes. When examining the flexibility of the two domains, we found that the N-terminal domain is more rigid than the C-terminal domain, which is a possible explanation for the one-way force propagation from the N-terminal Cys49-Cys57 bond to the C-terminal Cys186-Cys209 bond.

MATERIALS AND METHODS

MD simulations

All simulations were performed with Gromacs 4.5.x (27), the OPLS-AA force field (28,29), the tip4p water model (30), and 150 mM NaCl. We used three protein systems: TF(SS | SS) in the oxidized state (PDB: 1boy), TF(AA | SS), where Cys49 and Cys57 are mutated to alanines, and TF(SS | AA) where Cys186 and Cys209 are mutated to alanines. Simulation systems comprised dodecahedron boxes with ~150,000, ~130,000, and ~130,000 atoms, respectively. Periodic boundary conditions were used to remove artificial boundary effects. A cutoff of 1 nm was applied for Lennard-Jones interactions. Electrostatic interactions were calculated at a distance of <1 nm. Particle-mesh Ewald

summation was performed for long-range electrostatic interactions (31,32). The temperature was kept at 300 K with coupling to a Nosé-Hoover thermostat (33,34), and the coupling time was $\tau_t = 0.4$ ps. The pressure was kept at 1 bar using isotropic coupling to a Parrinello-Rahman barostat (35), with $\tau_p = 4.0$ ps and a compressibility of 4.5×10^{-5} bar^{-1}. Bonds including hydrogen atoms were constrained using the LINCS algorithm (36). An energy minimization using the steepest-descent algorithm was performed first; then, equilibration of the solvent with position restraints of 1.66 N/m on all protein heavy atoms was carried out. Finally, 100 ns simulations for each system (5000 frames for each simulation) were obtained. We then clustered conformations along the trajectories with a root mean-square distance (RMSD) cutoff of 1 Å. The top 10 most representative structures were selected for each system as new starting structures. Then, 10 independent 100 ns simulations were performed for each system, which resulted in 3.3 μs of trajectories in total.

FDA

FDA is a tool that is highly sensitive to changes in structures (21). For each frame, the pairwise forces, $\vec{F}_{i,j}$, between two atoms i and j were calculated according to the type of interaction between these two atoms in the force field. The cutoff was 1 nm. Non-bonded forces (Lennard Jones and electrostatic potentials) and bonded forces involving only two atoms were computed directly from the potential. Bonded forces involving more than two atoms (angles and proper and improper dihedral angles) were decomposed into pairwise atoms (21).

Pairwise forces between two residues, $\vec{F}_{ri,rj}$, can be obtained by summing up atomic forces between these two residues:

$$\vec{F}_{ri,rj} = \sum \vec{F}_{i,j}. \tag{1}$$

To measure the impact of ablation of disulfide bonds, subtraction of the pairwise forces between the oxidized state and the double-alanine mutants was calculated:

$$\Delta F_{ri,rj} = \left| \vec{F}_{\mathrm{re}_{ri,rj}} - \vec{F}_{\mathrm{ox}_{ri,rj}} \right|. \tag{2}$$

By summing up all the residue-based pairwise forces as scalars, the punctual stress of each residue was obtained:

$$\Delta F_{ri} = \sum_{rj=1}^{n} \Delta F_{ri,rj}. \tag{3}$$

Punctual stress has been used in several studies, and it measures the accumulation of forces at particles (residues/atoms) (21,37). It thus inherits the unit of force, pN. Visualizing stresses by color coding of protein structures allows us to identify mechanical hot spots.

To assess the influence of the mutations in the upper and lower disulfides, respectively, two force matrices, $\Delta F_{ri,rj}\,(\mathrm{AA}\,|\,\mathrm{SS}) = \left|\vec{F}_{\mathrm{AA}\,|\,\mathrm{SS}_{ri,rj}} - \vec{F}_{\mathrm{SS}\,|\,\mathrm{SS}_{ri,rj}}\right|$ and $\Delta F_{ri,rj}\,(\mathrm{SS}\,|\,\mathrm{AA}) = \left|\vec{F}_{\mathrm{SS}\,|\,\mathrm{AA}_{ri,rj}} - \vec{F}_{\mathrm{SS}\,|\,\mathrm{SS}_{ri,rj}}\right|$, were obtained from averaging >10 simulations. For each simulation, forces were calculated by averaging over the 5000 frames corresponding to 100 ns of simulated protein dynamics. The matrices were converted into networks. To this end, a vertex-count algorithm was employed to search for the largest connected network with a certain force cutoff. More specifically, we only kept edges with absolute force differences larger than the cutoff, and then searched for connected networks, i.e., groups of nodes connected by at least one edge (Fig. S1 in the Supporting Material). From these networks, the largest was chosen and visualized. For comparison, we chose cutoffs of 30, 50, 60, and 90 pN, and repeated the network analysis. This method has previously been successfully used to trace signal transduction in Hsp90 (23).

Shortest pathways

The vertex-count method gives an overview of all connected pairs with a significant response to perturbation. However, to identify residues in the allosteric pathways between the two disulfide bond positions, only $\Delta F_{ri,rj}\,(\mathrm{AA}\,|\,\mathrm{SS})$ matrices significantly larger than $\Delta F_{ri,rj}\,(\mathrm{SS}\,|\,\mathrm{AA})$ ($p < 0.05$ by the Wilcoxon rank-sum test (38)) were considered. A non-directed graph was built, and the reciprocals of the residue-based pairwise forces were used as weights for each pair. Dijkstra's algorithm (39) was employed to search for the shortest pathway with maximal likelihood from one residue to another residue. Yen's algorithm (40) then was applied to obtain the top 100 shortest pathways.

Force constant

To rationalize the asymmetric force distribution in TF, we estimated the flexibility of the two TF domains by Boltzmann inversion. Commonly, the distribution of the conformational ensemble for an equilibrium system follows the Boltzmann distribution,

$$P(x) \propto e^{-\frac{E}{k_B T}}, \tag{4}$$

where $P(x)$ is the probability of the ensemble being situated along a coordinate x (here, the radius of gyration), k_B is the Boltzmann constant, T is the temperature of the system (300 K), and E is the energy as a function of the radius gyration. We assume that E follows a harmonic function,

$$E(x) = \frac{1}{2}k(x - x_0)^2, \tag{5}$$

where x_0 is the equilibrium radius of the gyration and k is the force constant acting along the radius of gyration, which indicates the rigidity of the domain. According to Eqs. 4 and 5, the distribution of the radius of gyration can be fitted with a Gaussian distribution,

$$f(x) = \frac{1}{\sqrt{2\pi}\sigma_i} e^{-\frac{(x-x_0)^2}{2\sigma^2}}, \tag{6}$$

from which the force constant, k, can be estimated as

$$k = \frac{k_B T}{\sigma^2}, \tag{7}$$

where σ can be obtained by fitting the distribution of the radius of gyration of the two TF domains obtained from MD simulations according to Eq. 6. The distribution of the radii of gyration were calculated by counting the 10 simulations of the wild-type TF together (10 × 5000 frames).

RESULTS AND DISCUSSION

Structures and dynamics of the two disulfide bonds in TF

To examine the properties of the two disulfide bonds in oxidized TF (Fig. 1 *A*), we first analyzed the five dihedral angles of each disulfide bond to classify the bonds into geometric classes based on their signs. The distributions of five dihedral angles, χ_1, χ_2, χ_3, χ_2', and χ_1' over 50,000 frames shows that the configuration of the Cys49-Cys57 bond fluctuates widely (57.3% −RHSpiral, 13.7% ±RHSpiral, and 9.3% −LHSpiral in Fig. 1 *B* and Fig. S2 *A*). Conversely,

the distributions of the five dihedral angles of the Cys186-Cys209 disulfide are narrow and steadily remain within the signs of −, −, +, −, − (Fig. 1 *C*), which suggests that the Cys186-Cys209 disulfide remains a −RHStaple disulfide bond in equilibrium simulations (100% −RHStaple (Fig. S2 *B*)). The distributions of S-S lengths of the Cys186-Cys209 bond shifted toward longer lengths compared to the Cys49-Cys57 bond (Fig. 1 *D*). In addition, the C-S-S angles of the Cys186-Cys209 bond are significantly larger than those of the Cys49-Cys57 bond (Fig. 1 *E*). The total prestress (16,17) between two cysteine residues, including all interactions, does not show large differences between the Cys49-Cys57 bond and the Cys186-Cys209 bond, which both lie in the range from +100 pN to −100 pN. However, the bonded force of the Cys186-Cys209 bond is larger than that of the Cys49-Cys57 bond, with a force magnitude of ~−300 pN, whereas the nonbonded force is ~400 pN (Fig. 1 *F*). The same trend was observed previously for other −RHStaple disulfide bonds (16). Our results on the structural and dynamic properties of the Cys186-Cys209 bond thus confirm that the Cys186-Cys209 disulfide has a −RHStaple configuration, whereas the Cys49-Cys57 bond resembles a disulfide that is often of a structural nature.

Disulfide ablation causes minor structural changes

We next examined the effect of ablating the disulfide bonds in TF on its structure and dynamics. To this end, analogous to the experiments of Liang et al. (18), we introduced point mutations SS → AA one by one. We here denote the three systems as TF(SS | SS) (oxidized TF), TF(AA | SS) (N-terminal S-S-bond-reduced TF), and TF(SS | AA) (C-terminal S-S-bond-reduced TF).

Upon mutation of an allosteric disulfide bond to two alanines, one could expect structural rearrangements of the protein. We calculated the RMSD from the wild-type upon mutation, but observed RMSDs of only ~0.3 nm for the mutants, values highly similar to those of the wild-type (Fig. S3 *A*). Also, the RMS fluctuation (RMSF) did not differ between open and closed disulfides, suggesting that large-scale conformational changes, at least on the sub-microsecond timescale, are largely absent in TF (Fig. S3 *B*). Furthermore, the classifications of the disulfide bonds remain the same as in the wild-type, with the dominant −RHStaple of Cys186-Cys209 (Figs. S2 D and S3 C) and the wide distribution of dihedrals for Cys49-Cys57 being unaffected (Figs. S2 *C* and S3 *D*). Also, the S-S bond lengths (Fig. S3, *E* and *F*) and C-S-S angles (Fig. S3, *G* and *H*) displayed similar distributions after ablating the other disulfide bond.

Given that the global structural changes, as well as the geometry changes of the distant disulfide, are not significant between the wild-type TF(SS | SS) and the mutants, we analyzed changes right in the vicinity of the respective mutation. To this end, we applied the DSSP algorithm (41,42) to analyze differences in the secondary structures of TF(SS | SS), TF(AA | SS), and TF(SS | AA). The main changes of secondary structures after mutating one disulfide bond are found for residues 48–51 in TF(AA | SS) (Fig. 2 *A*). In TF(SS | SS) and TF(SS | AA), the main secondary structure of this short sequence is β-sheet. Interestingly, residues 48–51 in TF(AA | SS) changed to a loop configuration (Fig. 2, *A* and *B*). Thus, the Cys49-Cys57 bond assists the adjacent residues in forming the secondary structure, a β-strand, whereas the mutation Cys49Ala caused the adjacent residues to form a loop. Overall, the structural adaption was minor and was only detected locally around Cys49-Cys57 upon mutation.

N-terminal disulfide ablation stresses TF more widely

Monitoring the propagation of forces, a measure for perturbations more sensitive than coordinates, allows the detection of long-range allosteric communication. We here compared stresses in TF wild-type and mutants to reveal allosteric pathways upon removal of one of the disulfides. Using Eqs. 1, 2, and 3, we calculated punctual stresses of TF(AA | SS) and TF(SS | AA) relative to TF(SS | SS). Remarkably, ablation of the disulfide bond Cys49-Cys57 induced mechanical changes in the C-terminal domain. Instead, punctual stresses in the N-terminal domain are low in both TF(AA | SS) and TF(SS | AA) (Fig. 3 *A*). Specifically, the punctual stress in the Cys186-Cys209 bond upon ablating the N-terminal disulfide, i.e., when subtracting the stresses of TF(AA | SS) from those of TF(SS | SS), was in the range 200–300 pN, whereas the punctual stress in Cys49-Cys57, when subtracting TF(SS | AA) stresses from those of TF(SS | SS), was in the range 80–150 pN (Fig. 3 *C*). This demonstrates that the mechanical impact of the N-terminal mutation, Cys49Ala-Cys57Ala, on the C-terminal disulfide bond, Cys186-Cys209, is twice as high as the impact of the C-terminal mutation, Cys186Ala-Cys209Ala, on the Cys49-Cys57 bond.

To quantify the stress changes more globally throughout TF, we averaged stress over the secondary structure blocks of TF(SS | SS) as a reference (the assignment of the secondary structure is shown in Table S1) (43). The sites featuring main changes in both TF(AA | SS) and TF(SS | AA) in comparison to TF(SS | SS) are 1) the loop between $\beta 9_B$ and $\beta 10$ near the intermediate interface, through which the signal is transduced between the two domains; 2) the $\alpha 3$ helix, also located at the interface, a change that is also confirmed by our force network and pathway analyses in the next sections; and 3) the two β-strands where the Cys186-Cys209 bond is located, $\beta 15_F$ and $\beta 16_G$ (Fig. 3). As already noted, most of the changes occurred in the C-terminal domain instead of the N-terminal domain. Remarkably, in TF(AA | SS), there was a large change in $\beta 5_E$ around

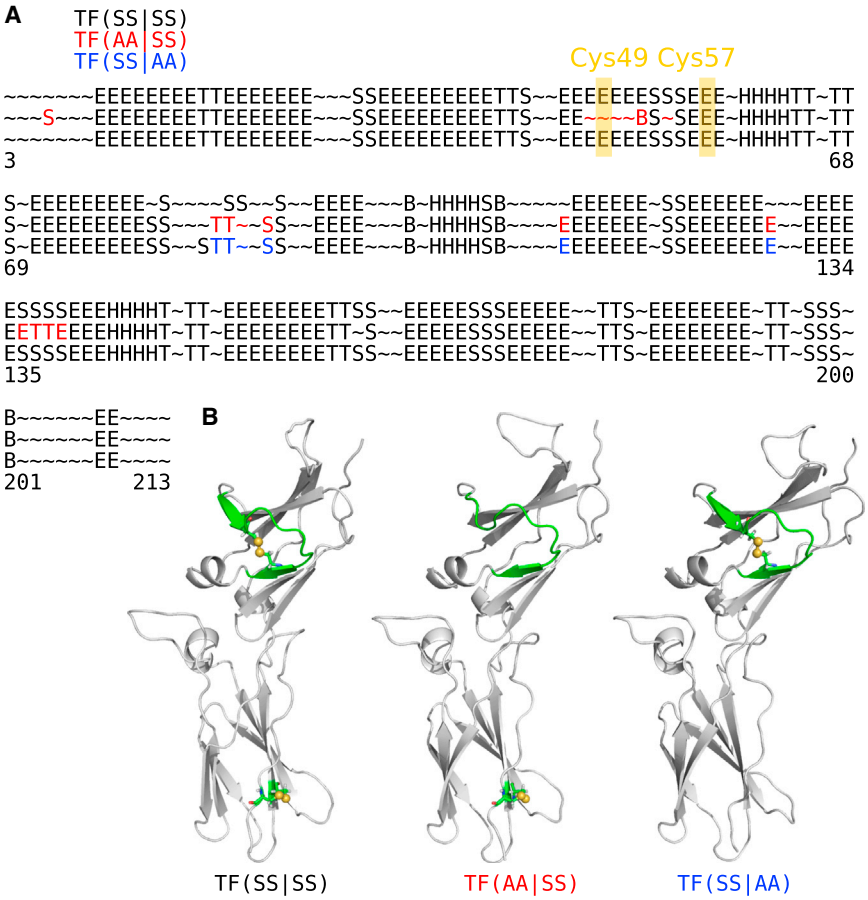

FIGURE 2 Secondary-structure analysis upon disulfide ablation. For each amino acid from the N-terminus to the C-terminus of TF, the dominant secondary structure is given. Eight types of secondary structure were assigned: the coil (~), the β-sheet (E), the β-bridge (B), the bend (S), the turn (T), the α-helix (C), the 5-helix (I), and the 3-helix (H). If one type of secondary-structure element is sampled by a particular amino acid in >50% of all frames, that secondary-structure type is assigned to that amino acid. If no secondary-structure elements have a high ratio, the coil structure (~) will be assigned. (*A*) The differences between TF(AA | SS) and TF(SS | SS) are highlighted in red and the differences between TF(SS | AA) and TF(SS | SS) in blue. The disulfide bonded cysteines are yellow. (*B*) Cartoon representation of wild-type TF and the mutants, with residues 46–58, 186, and 209 highlighted in green. To see this figure in color, go online.

Cys57 relative to TF(SS | SS) (Fig. 3 *B*, *left*, and Fig. 3 *D*). Although the punctual stress of $\beta 4_{C'}$ is not in the top 10 high punctual stresses for the TF(AA | SS), it still showed a punctual stress as high as ~300 pN (Fig. 3 *D*). The high punctual stresses near Cys49-Cys57 agree with the secondary structural changes (Fig. 2). Thr101, located right behind the Cys49-Cys57 bond, stored high punctual stress upon mutation of the distant Cys186Ala-Cys209Ala (Fig. 3 *B*, *right*, and Fig. 3 *E*).

Force network connects disulfides

Having established that there is a larger response to the abolishment of the N-terminal disulfide bond than to the abolishment of the C-terminal bond, we next investigated how the perturbation upon mutation is transduced through the two-domain TF. The punctual stress indicated the influence of the mutations on specific residues and secondary-structure elements. The connected pairwise force network allows us to compare the paths of force propagation in TF(AA | SS) and TF(SS | AA). The force network propagated from the Cys49-Cys57 disulfide to the Cys186-Cys209 disulfide with a cutoff of 50 pN, and to the N-terminal loop with a cutoff of 30 pN (Fig. 4 *A*) after mutating the Cys49-Cys57 disulfide to alanines. Conversely, the force network did not spread from the Cys186-Cys209 disulfide to the Cys49-Cys57 disulfide with either cutoff, 30 or 50 pN (Fig. 4 *B*). However, the force propagated from the Cys186-Cys209 disulfide to regions in the N-terminal domain distant from the Cys49-Cys57 bond in TF(SS | AA) (cutoffs of 30, 50, and 60 pN in Fig. 4 *B*). This observation confirmed the accumulation of high punctual stress at Thr101 (Fig. 3, *B*, right, and E).

This result, together with the punctual stress analysis, is in accordance with the experimental observation that the ablation of the Cys49-Cys57 disulfide changes the redox potential of the Cys186-Cys209 bond, but not vice versa (18). Here, we propose that this redox communication between the two disulfide bonds in TF is the consequence of a one-way force propagation mechanism. Interestingly, no matter which disulfide bond was mutated, the force propagation always involved the α-helix $\alpha 3$ at the interface between the N-terminal and C-terminal domains, even for a high cutoff of 90 pN (Fig. 4, *A* and *B*). One explanation is that the $\alpha 3$ helix establishes an indispensable link between the N-terminal and C-terminal domains.

One-way force propagation pathway

We further characterized the one-way propagation by calculating the shortest pathway from the Cys49-Cys57 bond to

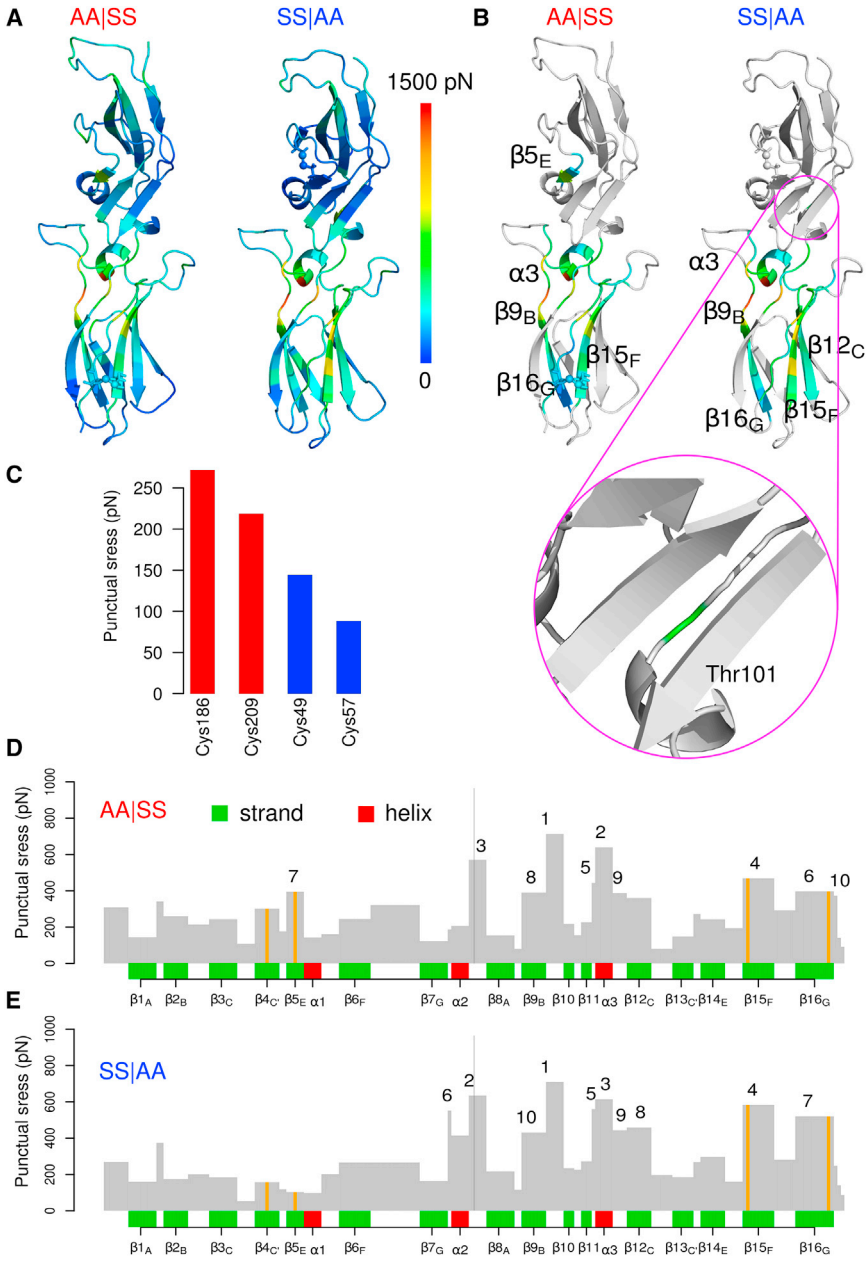

FIGURE 3 Punctual stresses upon disulfide ablation. (*A*) Stress distribution (ΔF_{ri}) upon mutation in the N-terminal domain (TF(AA | SS), *left*) and in the C-terminal domain (TF(SS | AA), *right*). (*B*) Similar to (*A*), but with secondary-structure elements (Table S1) with particular stress levels labeled according to the system in (*D*) and (*E*). (*C*) Punctual stress of the cysteine residues for the two disulfide bonds, Cys186 and Cys209 in TF(AA | SS) and Cys49 and Cys57 in TF(SS | AA). (*D* and *E*) Punctual stress averaged over each secondary-structure element in TF(AA | SS) and TF(SS | AA), with green for β-strands, red for helixes, and orange for sites of cysteine residues. The TF sequence comprises residues 3–213 from left (N-terminus) to right (C-terminus). The upper domain (residues 3–107) and the lower domain (residues 108–213) are separated by the black line. To see this figure in color, go online.

the Cys186-Cys209 bond after ablating the disulfide bond Cys49-Cys57 with Dijkstra's algorithm (Fig. S4 *A*). The pairwise force differences upon ablating the Cys49-Cys57 disulfide bond, $\Delta F\ (\mathrm{AA}\,|\,\mathrm{SS}) = F_{\mathrm{TF(AA|SS)}} - F_{\mathrm{TF(SS|SS)}}$ of residues participating in the shortest path are compared to the same differences upon ablating the Cys186-Cys209 bond, $\Delta F\ (\mathrm{SS}\,|\,\mathrm{AA}) = F_{\mathrm{TF(SS\,|\,AA)}} - F_{\mathrm{TF(SS\,|\,SS)}}$ in Fig. S4 *B*. For most pairwise forces, $\Delta F\ (\mathrm{AA}\,|\,\mathrm{SS})$ is of larger magnitude than $\Delta F\ (\mathrm{SS}\,|\,\mathrm{AA})$.

However, focusing on one single force-propagation pathway may cause us to miss the possibility of alternative side paths. We calculated the top 100 shortest pathways using Yen's algorithm (Fig. 5, *A* and *B*). The path spans $\beta4_{C'}$-$\beta5_E$-$\alpha1$-$\beta2_B$-$\alpha2$-loop-$\alpha3$—loop-$\beta9_B$-$\beta12_C$-$\beta15_F$-$\beta16_G$ (Fig. 5 *A*). High forces $\Delta F_{ri,rj}$ (AA | SS), as expected, include the pair between the Cys49Ala and the Cys57Ala, a direct effect of the mutation, which suggests that Cys49-Cys57 plays an important structural role in linking the two β-strands $\beta4_{C'}$ and $\beta5_E$. This finding also agrees with the secondary structure changes (residues 48–51 in Fig. 2) and high punctual stresses at $\beta4_{C'}$ and $\beta5_E$ (Fig. 3). High forces are also observed, which was similarly emphasized by the punctual stress (Fig. 3) and, remarkably, near the Cys186-Cys209 disulfide bond. Even though $\Delta F_{186,209}$ between TF(AA | SS) and TF(SS | SS) is low, pairwise interaction of this disulfide bond with its environment resulted in a high punctual stress at Cys186 and Cys209 (Fig. 3 *C*). Between the N-terminal domain and the C-terminal domain,

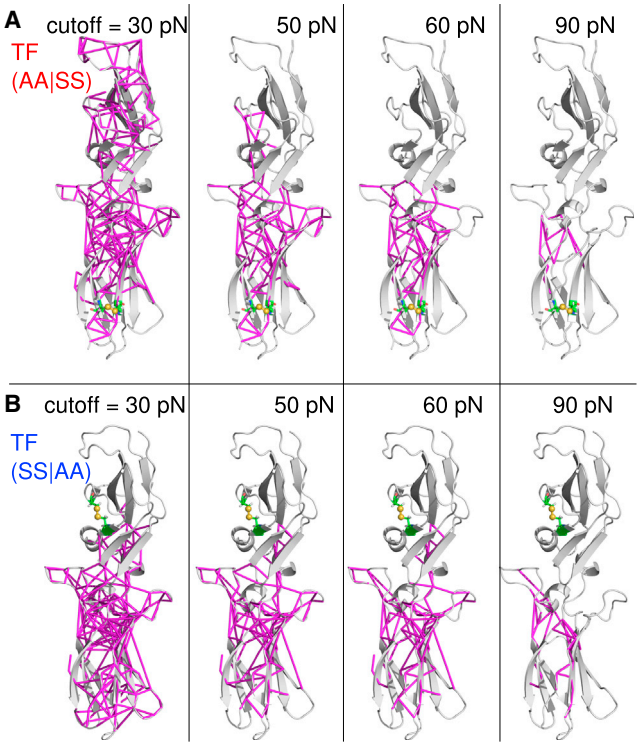

FIGURE 4 Residue-based pairwise force network. Connected network for (*A*) TF(AA | SS) and (*B*) TF(SS | AA) with different cutoffs: 30 pN, 50 pN, 60 pN, and 90 pN. To see this figure in color, go online.

there are four residue pairs carrying high forces involving Phe19, Thr132, Leu143, Tyr103, Val146, and Phe147 (Fig. 5 *B*). Therefore, we suggest these residues as mutation candidates to test our proposed one-way force propagation.

Asymmetric allostery through different domain stiffnesses

We here found evidence for one-way force propagation from the N-terminal to the C-terminal domain by ablating the N-terminal disulfide bond, and we pointed to the interdomain interface as playing a particular role as a force distribution "hub". However, what drives the particular one-way force propagation intrinsically? To answer this question, we assessed the different flexibility of the domains in terms of their radii of gyration. The radius of gyration for the C-terminal domain can be fitted well with a Gaussian distribution, whereas for the N-terminal domain, the distribution did not follow a Gaussian shape (Fig. 6). RMSD calculations suggested that the loop at the end of the C-terminus is highly flexible, and its flexibility could dominate the distribution of the radius of gyration. To remove the influence from loop dynamics, we calculated the radius of gyration without residues 77–91. We then obtained standard deviations for the radius of gyration of 0.008 nm and 0.0145 nm for the N-terminal and C-terminal domains,

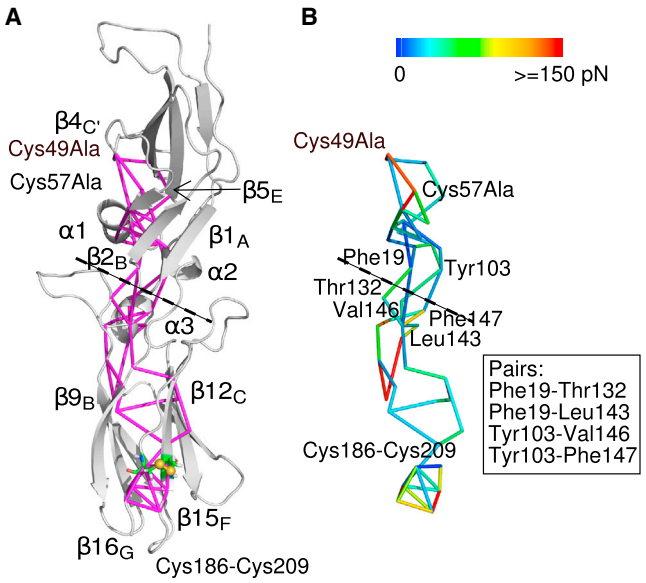

FIGURE 5 Top 100 shortest force-propagation pathways from Cys49-Cys186 to Cys186-Cys209 after ablating the disulfide bond Cys49-Cys57. (*A*) The pathways are visualized as magenta sticks within the TF structure. Secondary-structure elements involved in force propagation are indicated. The dashed line shows the domain interface. (*B*) Same as in (*A*), but color coded by residue-pairwise force differences, ΔF (AA | SS). To see this figure in color, go online.

respectively. Under the assumption of a harmonic potential along the radius-of-gyration coordinate, and using Boltzmann inversion (Eq. 7), we obtained corresponding force constants of 57 N/m and 20 N/m. This estimation suggests that the N-terminal domain is more rigid than the C-terminal domain, which explains the one-way force propagation mechanism: when the disulfide bond Cys49-Cys57 in the rigid N-terminal domain is mutated, the force is efficiently propagated to the softer C-terminal domain; thus, the redox potential of the Cys186-Cys209 bond is changed. However,

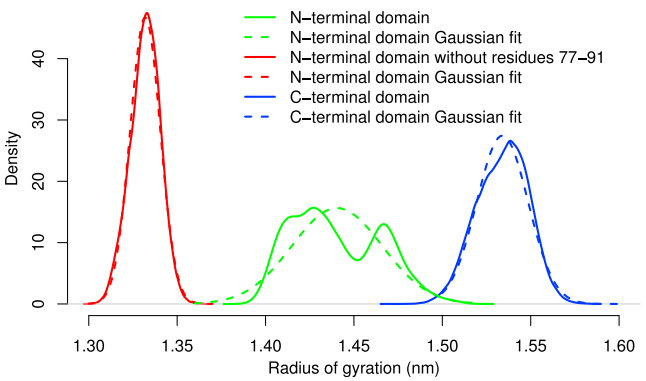

FIGURE 6 Radius-of-gyration distribution for the two domains. Solid lines indicate data from MD simulations of wild-type TF for the N-terminal domain (*green*), the same domain without taking the loop 77–91 into account (*red*), and the C-terminal domain (*blue*). The Gaussian fits allow us to estimate the domain rigidity (*dashed lines*). To see this figure in color, go online.

the mutation of the disulfide bond Cys186-Cys209 in the soft C-terminal domain only induces perturbations within the floppy C-terminal domain (Fig. 3 *A*). The softer domain shows a larger tendency to dissipate the perturbation, which for this reason is rather short-range.

CONCLUSION

Our MD simulations confirmed the allosteric communication between the two disulfide bonds in TF. FDA, together with the network and pathway methods, revealed a mechanical pathway from the N-terminal to the C-terminal domain. The estimation of the domain force constants provided an explanation, namely a large difference in stiffness, which might be a common mechanism of allostery of proteins. However, the radius of gyration is only one of the parameters that can indicate the stiffness of protein domains. Additionally, the extent of collective motions or conformational entropies might serve as valuable alternative measures.

The biological relevance of our findings for TF function is uncertain. Ablation of the N-terminal disulfide bond in cellular TF by replacing both cysteines with serines does not affect TF pro-coagulant activity (10). It is interesting to note, however, that the N-terminal disulfide bond was found to exist in oxidized and reduced forms in one of the crystal structures (11,43). It is possible that the N-terminal disulfide controls the redox state of the C-terminal bond and thus TF bioactivity. Independent of these considerations, our results propose differential domain stiffness for one-way communication in proteins as a mechanism potentially at play beyond TF.

In this study, we have confirmed the impact on the C-terminal domain by ablating the N-terminal disulfide, including local conformational changes in the N-terminal domain. Instead, ablating the strained C-terminal −RHStaple disulfide bond shows no long-range allosteric effects either experimentally or theoretically. Similarly, no obvious structural changes were observed upon reducing the −RHStaple disulfide bonds in either CD4 and vWFC1 in our previous study (16). Although longer-timescale MD simulations may allow us to observe large conformational changes, the stability of antiparallel β-strands near the −RHStaple disulfide suggests that this disulfide is a regulatory switch with rather local consequences instead of a trigger for large conformational changes. Coagulation activity of TF has been shown to require the formation of the C-terminal −RHStaple bond. Our data suggest that FVII binding to TF, the first step of coagulation initiation, involves direct detection of the disulfide instead of disulfide-dependent structural changes elsewhere in TF.

We have proposed mutation candidates near the interface between the two domains. Simulations with mutants of these residues, or experiments to test redox potential changes can further verify the asymmetric allosteric communication. The highly sensitive FDA, combined with network and pathway analyses, is a useful tool for redox-mediated allostery in the systems increasingly revealed to be regulated by functional disulfides (12–14,44,45).

SUPPORTING MATERIAL

Four figures and one table are available at http://www.biophysj.org/biophysj/supplemental/S0006-3495(16)34277-1.

AUTHOR CONTRIBUTIONS

P.H. and F.G. conceived the project; B.Z. performed the simulations and analyzed the results; and B.Z., F.G., and P.H. wrote the article.

ACKNOWLEDGMENTS

We thank Dr. Camilo Aponte-Santamaria for his valuable suggestions.

This work was supported by the Klaus Tschira Foundation, the Max Planck Gesellschaft-Chinese Academy of Sciences joint doctoral promotion programme (B.Z.), Deutsche Forschungsgemeinschaft (DFG) grant GR 3494/2-1 (F.G.), and the DFG research group FOR1543, "Shear flow regulation of hemostasis: bridging the gap between nanomechanics and clinical presentation" (F.G.).

REFERENCES

1. Chen, V. M., and P. J. Hogg. 2013. Encryption and decryption of tissue factor. *J. Thromb. Haemost.* 11 (*Suppl 1*):277–284.
2. Wang, P., Y. Wu, …, L. Zhong. 2013. Thioredoxin and thioredoxin reductase control tissue factor activity by thiol redox-dependent mechanism. *J. Biol. Chem.* 288:3346–3358.
3. Reinhardt, C., M.-L. von Brühl, …, B. Engelmann. 2008. Protein disulfide isomerase acts as an injury response signal that enhances fibrin generation via tissue factor activation. *J. Clin. Invest.* 118:1110–1122.
4. Ahamed, J., H. H. Versteeg, …, W. Ruf. 2006. Disulfide isomerization switches tissue factor from coagulation to cell signaling. *Proc. Natl. Acad. Sci. USA.* 103:13932–13937.
5. Van den Hengel, L. G., S. Osanto, …, H. H. Versteeg. 2013. Murine tissue factor coagulant activity is critically dependent on the presence of an intact allosteric disulfide. *Haematologica.* 98:153–158.
6. Langer, F., and W. Ruf. 2014. Synergies of phosphatidylserine and protein disulfide isomerase in tissue factor activation. *Thromb. Haemost.* 111:590–597.
7. Chiu, J., F. Passam, …, P. J. Hogg. 2015. Protein disulfide isomerase in thrombosis. *Semin. Thromb. Hemost.* 41:765–773.
8. Versteeg, H. H., C. A. Spek, …, D. J. Richel. 2004. Tissue factor and cancer metastasis: the role of intracellular and extracellular signaling pathways. *Mol. Med.* 10:6–11.
9. Harlos, K., D. M. Martin, …, C. W. Boys. 1994. Crystal structure of the extracellular region of human tissue factor. *Nature.* 370:662–666.
10. Rehemtulla, A., W. Ruf, and T. S. Edgington. 1991. The integrity of the cysteine 186-cysteine 209 bond of the second disulfide loop of tissue factor is required for binding of factor VII. *J. Biol. Chem.* 266:10294–10299.
11. Schmidt, B., L. Ho, and P. J. Hogg. 2006. Allosteric disulfide bonds. *Biochemistry.* 45:7429–7433.
12. Cook, K. M., and P. J. Hogg. 2013. Post-translational control of protein function by disulfide bond cleavage. *Antioxid. Redox Signal.* 18:1987–2015.
13. Hogg, P. J. 2013. Targeting allosteric disulphide bonds in cancer. *Nat. Rev. Cancer.* 13:425–431.

14. Butera, D., K. M. Cook, …, P. J. Hogg. 2014. Control of blood proteins by functional disulfide bonds. *Blood.* 123:2000–2007.
15. Butera, D., T. Wind, …, P. J. Hogg. 2014. Characterization of a reduced form of plasma plasminogen as the precursor for angiostatin formation. *J. Biol. Chem.* 289:2992–3000.
16. Zhou, B., I. B. Baldus, …, F. Gräter. 2014. Identification of allosteric disulfides from prestress analysis. *Biophys. J.* 107:672–681.
17. Edwards, S. A., J. Wagner, and F. Gräter. 2012. Dynamic prestress in a globular protein. *PLOS Comput. Biol.* 8:e1002509.
18. Liang, H. P., T. M. Brophy, and P. J. Hogg. 2011. Redox properties of the tissue factor Cys186-Cys209 disulfide bond. *Biochem. J.* 437:455–460.
19. Liu, J., and R. Nussinov. 2016. Allostery: an overview of its history, concepts, methods, and applications. *PLOS Comput. Biol.* 12:e1004966.
20. Hertig, S., N. R. Latorraca, and R. O. Dror. 2016. Revealing atomic-level mechanisms of protein allostery with molecular dynamics simulations. *PLOS Comput. Biol.* 12:e1004746.
21. Costescu, B. I., and F. Gräter. 2013. Time-resolved force distribution analysis. *BMC Biophys.* 6:5.
22. Louet, M., C. Seifert, …, F. Gräter. 2015. Dynamic allostery of the catabolite activator protein revealed by interatomic forces. *PLOS Comput. Biol.* 11:e1004358.
23. Seifert, C., and F. Gräter. 2012. Force distribution reveals signal transduction in *E. coli* Hsp90. *Biophys. J.* 103:2195–2202.
24. Stacklies, W., F. Xia, and F. Gräter. 2009. Dynamic allostery in the methionine repressor revealed by force distribution analysis. *PLOS Comput. Biol.* 5:e1000574.
25. Stacklies, W., M. C. Vega, …, F. Gräter. 2009. Mechanical network in titin immunoglobulin from force distribution analysis. *PLOS Comput. Biol.* 5:e1000306.
26. Stacklies, W., C. Seifert, and F. Graeter. 2011. Implementation of force distribution analysis for molecular dynamics simulations. *BMC Bioinformatics.* 12:101.
27. Hess, B., C. Kutzner, …, E. Lindahl. 2008. GROMACS 4: Algorithms for highly efficient, load-balanced, and scalable molecular simulation. *J. Chem. Theory Comput.* 4:435–447.
28. Jorgensen, W. L., D. S. Maxwell, and J. Tirado-Rives. 1996. Development and testing of the OPLS all-atom force field on conformational energetics and properties of organic liquids. *J. Am. Chem. Soc.* 118:11225–11236.
29. Kaminski, G. A., R. A. Friesner, …, W. L. Jorgensen. 2001. Evaluation and reparametrization of the OPLS-AA force field for proteins via comparison with accurate quantum chemical calculations on peptides. *J. Phys. Chem. B.* 105:6474–6487.
30. Jorgensen, W. L., J. Chandrasekhar, …, M. L. Klein. 1983. Comparison of simple potential functions for simulating liquid water. *J. Chem. Phys.* 79:926–935.
31. Darden, T., D. York, and L. Pedersen. 1993. Particle mesh Ewald: An N log(N) method for Ewald sums in large systems. *J. Chem. Phys.* 98:10089–10092.
32. Essmann, U., L. Perera, …, L. G. Pedersen. 1995. A smooth particle mesh Ewald method. *J. Chem. Phys.* 103:8577–8593.
33. Nosé, S. 1984. A unified formulation of the constant temperature molecular dynamics methods. *J. Chem. Phys.* 81:511–519.
34. Hoover, W. G. 1985. Canonical dynamics: equilibrium phase-space distributions. *Phys. Rev. A Gen. Phys.* 31:1695–1697.
35. Parrinello, M., and A. Rahman. 1981. Polymorphic transitions in single crystals: a new molecular dynamics method. *J. Appl. Phys.* 52:7182–7190.
36. Hess, B., H. Bekker, …, J. Fraaije. 1997. LINCS: a linear constraint solver for molecular simulations. *J. Comput. Chem.* 18:1463–1472.
37. Palmai, Z., C. Seifert, …, E. Balog. 2014. An allosteric signaling pathway of human 3-phosphoglycerate kinase from force distribution analysis. *PLOS Comput. Biol.* 10:e1003444.
38. Bauer, D. F. 1972. Constructing confidence sets using rank statistics. *J. Am. Stat. Assoc.* 67:687–690.
39. Dijkstra, E. W. 1959. A note on two problems in connexion with graphs. *Numer. Math.* 1:269–271.
40. Yen, J. Y. 1971. Finding the k shortest loopless paths in a network. *Manage. Sci.* 17:712–716.
41. Kabsch, W., and C. Sander. 1983. Dictionary of protein secondary structure: pattern recognition of hydrogen-bonded and geometrical features. *Biopolymers.* 22:2577–2637.
42. Joosten, R. P., T. A. te Beek, …, G. Vriend. 2011. A series of PDB related databases for everyday needs. *Nucleic Acids Res.* 39:D411–D419.
43. Muller, Y. A., M. H. Ultsch, and A. M. de Vos. 1996. The crystal structure of the extracellular domain of human tissue factor refined to 1.7 Å resolution. *J. Mol. Biol.* 256:144–159.
44. Metcalfe, C., P. Cresswell, …, A. N. Barclay. 2011. Labile disulfide bonds are common at the leucocyte cell surface. *Open Biol.* 1:110010.
45. Leonard, S. E., and K. S. Carroll. 2011. Chemical "omics" approaches for understanding protein cysteine oxidation in biology. *Curr. Opin. Chem. Biol.* 15:88–102.